CT-based radiomics combined with clinical features for invasiveness prediction and pathological subtypes classification of subsolid pulmonary nodules

Miaozhi Liu [a,1], Rui Duan [b,1], Zhifeng Xu [b,1], Zijie Fu [a], Zhiheng Li [a], Aizhen Pan [b,*], Yan Lin [a,**]

[a] Radiology Department, Second Affiliated Hospital of Shantou University Medical College, Shantou, Guangdong Province 515041, PR China
[b] Department of Radiology, First People's Hospital of Foshan, Foshan, Guangdong Province 528000, PR China

ARTICLE INFO

ABSTRACT

Purpose: To construct optimal models for predicting the invasiveness and pathological subtypes of subsolid nodules (SSNs) based on CT radiomics and clinical features.
Materials and Methods: This study was a retrospective study involving two centers. A total of 316 patients with 353 SSNs confirmed as atypical adenomatous hyperplasia (AAH), adenocarcinoma in situ (AIS), minimally invasive adenocarcinoma (MIA) and invasive adenocarcinoma (IAC) were included from January 2019 to February 2023. Models based on CT radiomics and clinical features were constructed for classification of AAH/AIS and MIA, MIA and IAC, as well as lepidic-predominant adenocarcinoma (LPA) and acinar-predominant adenocarcinoma (APA). Receiver operating characteristic (ROC) curve was used to evaluate the model performance. Finally, the nomograms based on the optimal models were established.
Results: The nomogram based on the combined model (AAH/AIS versus MIA) consisting of lobulation, the GGN-vessel relationship, diameter, CT value, consolidation tumor ratio (CTR) and rad-score performed the best (AUC=0.841), while age, CT value, CTR and rad-score were the significant features for distinguishing MIA from IAC, the nomogram based on these features performed the best (AUC=0.878). There were no significant differences in clinical features between LPA and APA, while the radiomics model based on rad-score showed good performance for distinguishing LPA from APA (AUC=0.926).
Conclusions: The nomograms based on radiomics and clinical features could predict the invasiveness of SSNs accurately. Moreover, radiomics models showed good performance in distinguishing LPA from APA.

1. Introduction

Lung cancer is the second most common cancer and the leading cause of cancer death worldwide [1]. The most common pathological type of lung cancer is adenocarcinoma [2], which can be pathologically categorized into adenomatous precursor lesions (APL), microinvasive adenocarcinoma (MIA) and invasive adenocarcinoma (IAC). APL was further classified into atypical adenomatous hyperplasia (AAH) and adenocarcinoma in situ (AIS), which is regarded as pre-invasive lesions. [3]. APLs often have good biological behavior and long-term unchanged, which can be followed up to select the best surgical timepoint and reducing the overtreatment [4,5] . MIA is a newly defined subtype of lung adenocarcinoma that does not invade the lymphatic vessels, blood vessels, or pleura [6]. Previous studies show that the disease-free survival (DFS) rate after surgery for patients with MIA is reportedly almost 100 % [7,8] . Different from MIA, IAC is the final stage in the transformation of lung cancer, which is characterized by invasion of the pleura and airway, invasion of blood vessels and lymphatics, tumor necrosis, airway transmission and worse prognosis compared to MIA [9]. In addition, IAC is further categorized into five subtypes: lepidic predominant adenocarcinoma (LPA), acinar predominant adenocarcinoma (APA), papillary predominant adenocarcinoma (PAP), micropapillary predominant adenocarcinoma (MPA) and solid predominant adenocarcinoma (SPA), and the prognosis and therapeutic interventions

of different subtypes of IAC are different. LPA has the best prognosis with a very low risk of recurrence, while APA and PAP have a moderate risk of recurrence. MPA and SPA have a higher probability of lymph node metastasis and postoperative recurrence [10]. Therefore, early detection of invasiveness and subtype classification are critical for optimal decision-making in patients with early-stage adenocarcinoma. Intraoperative freezing is the routine practice to assess the invasiveness of pulmonary nodules in clinic, but its accuracy is probably limited due to the different diagnostic levels of pathologists and inadequate sampling [11,12]. Currently, computed tomography (CT) has played a crucial role in the preoperative assessment of the invasiveness of pulmonary nodules [13]. With the increasing use of CT screening and artificial intelligence, more and more pulmonary subsolid nodules (SSNs) (including pure ground glass nodules (pGGNs) and mixed ground glass nodules (mGGNs)) were found. Most of the SSNs are the early manifestation of lung adenocarcinoma. Considering the considerable overlap of CT imaging features among various histological subtypes [14, 15], it is difficult to identify histological invasiveness with the CT imaging features alone.

As an emerging discipline of mining high-throughput data from medical images, radiomics has great potential for identifying the heterogeneity of early-stage lung adenocarcinomas [16,17]. Previous studies proved that radiomics-based models could improve the performance of identifying the invasiveness of pulmonary nodules [18,19]. However, there are currently few studies on invasiveness prediction of SSN and subtypes classification of IAC.

Thus, the purpose of this study was to establish models for invasiveness prediction (AAH/AIS versus MIA and MIA versus IAC) of SSNs and subtypes classification of IAC in the early stage based on CT radiomics and clinical features, which is of great significance for the formulation of follow-up strategy and the selection of surgical protocols.

2. Materials and methods

2.1. Patients

This retrospective study was approved by the Ethics Committees of the two centers, and the requirement for informed consent was waived due to the retrospective nature of the study. From January 2019 to February 2023, the chest CT data of patients with SSNs were collected. The inclusion criteria were as follows: (1) lesions presenting as SSNs less than 3 cm in diameter; (2) nodules pathologically determined to be AAH, AIS, MIA, or IAC by surgical resection; and (3) the time interval between CT and surgery of less than one month. Exclusion criteria were as follows: (1) absence of thin-section CT images (0.625–1.25 mm); (2) poor-quality images that affects image segmentation; and (3) patients with experience of chemotherapy or radiotherapy.

2.2. CT imaging protocol

All patients received routine non-enhanced CT. The scanning features and corresponding reconstruction parameters were listed in Table S1. CT scans were obtained for all patients in the supine position at full inspiration.

2.3. Clinical factors and CT imaging features

The clinical factors included age, gender and smoke. The CT imaging features included diameter, CT value, lobulation (absent, present), spiculation (absent, present), pleural indentation (absent, present), vacuole sign (absent, present), crescent sign[20] (absent, present), air bronchogram (absent, present), solid component (absent, present), solid component size, consolidation tumor ratio (CTR): consolidation tumor size/diameter[21] and the GGN-vessel relationship (I~IV): type I (pass-by), vessels passed by GGNs without detectable supplying branches to lesions; type II (pass-through), vessels passed through the

lesions without obvious morphological changes in traveling path or size; type III (distorted/dilated), vessels within lesions were tortuous or rigid without an increase in amount; type IV (complicated), more complicated vasculature other than described in the aforementioned types within GGNs, for instance, coexistence of irregular vascular dilation and vascular convergence from multiple supplying vessels[22]. The imaging features were evaluated by two radiologists (with at least three years of experience in thoracic interpretation), and disagreements were resolved under the guidance of a senior radiologist with 20 years of experience in chest CT diagnosis.

2.4. Image preprocessing and nodule segmentation

Format conversion, bias field correction, and normalization were performed on all images using the open source Python 3.7 data package after acquiring raw CT data from patients (Figure S1). Then these preprocessed images were imported into 3D slicer software (version 4.11; National Institutes of Health; https://www.slicer.org, America) to adjust the unified grayscale parameters. Nodules were first segmented manually using the 3D slicer software by drawing a region of interest (ROI) along the boundary of each nodule on the CT images slice by slice until the entire nodule had been covered.

2.5. Radiomics feature extraction, standardization

Shape Features, First Order Features, Gray Level Co-occurrence Matrix (GLCM) Features, Gray Level Size Zone (GLSZM) Features, Gray Level Run Length Matrix (GLRLM) Features and Gray Level Dependence Matrix (GLDM) Features were computed automatically extracted by utilizing the pyradiomics (https://pyradiomics.readthedocs.io/en/latest). Z-scores was used to standardize all radiomics features. ComBaTool (https://forlhac.shinyapps.io/Shiny_ComBat/) was used to address batch effects and principal component analysis (PCA) was used to visualize the correction of batch effects on these features by ComBats.

2.6. Prediction modeling

2.6.1. Clinical model construction
The clinical model was based on the clinical factors and CT imaging features. Univariate analyses were conducted on all clinical factors and CT imaging features in the training set. A multivariate analysis was performed by the logistic regression analysis to build the clinical model with the significant variables resulting from the univariate analysis.

2.6.2. Radiomics feature selection and model construction
Two experienced radiologists independently segmented the ROIs of CT data of 50 randomly selected nodules without any clinical information. After that, we analyzed the interobserver reproducibility of the feature extraction. Radiomics features with good interobserver reproducibility (intraclass correlation coefficient [ICC]≥0.80) were included in subsequent analyses. Then, two feature selection methods, maximum relevance–minimum redundancy (mRMR) and least absolute shrinkage and selection operator (LASSO), were used to select the features. Firstly, mRMR was performed to eliminate the redundant and irrelevant features and 30 features were retained. Secondly, LASSO was conducted to choose the optimized subset of features to construct the final model (The optimal parameter (λ.min) was selected by ten-fold cross-validation). Finally, radiomics score (rad-score) was calculated by summing the selected features weighted by their coefficients.

2.6.3. Combined model construction and nomogram development
The combined model, built by multivariate logistic regression analysis, was based on the combination of the significant clinical features and rad-score. A nomogram was established based on the optimal model found in the training set.

2.7. Model evaluation and clinical utility

The performance of the clinical model, radiomics model, and the combined model in the training set and test set were evaluated by utilizing the receiver operating characteristic (ROC) curve and the area under the curve (AUC) on Med Calc 18.2.1 (America). Moreover, we draw a nomogram to visualize the optimal model.

2.8. Statistical analysis

All statistical analyses in this study were performed with R software (version 3.6.2, America). Normally distributed variables were analyzed by the Students' t-test, while non-normally distributed continuous variables were calculated by means of the Mann–Whitney U test. The chi-square test was used to compare categorical variables. The DeLong's test was used to compare the area under ROC curves of different models. A two-sided P value < 0.05 was considered statistically significant.

3. Results

3.1. Clinicopathological findings

A total of 353 SSNs in 316 patients from two centers were included,

which were divided into AAH/AIS (n=106) group, MIA (n=160) group and IAC (n=87) group. IAC group were further divided into LPA (n=42) group and APA (n=36) group [SSNs confirmed as PAP (n=9) were excluded in this study due to small samples; MPA and SPA was not observed in this study]. All 353 SSNs from two centers were randomly divided with the ratio of 7:3 for training set and test set. The flowchart of study population was shown in Fig. 1.

3.2. Radiomics feature extraction, standardization

A total of 1218 radiomics features were extracted. Figure S2 shows that ComBat standardization aggregated the distributions of data from the two centers, which were scattered before addressing the center effects.

3.3. SSNs invasiveness prediction model construction

3.3.1. Clinical model

With regards to the clinical factors and CT imaging features, the univariate analysis showed that diameter, CT value, lobulation, spiculation, the GGN-vessel relationship, solid component and CTR were significantly different in the training set between AAH/AIS group and MIA group (Table 1). Multivariate analysis further revealed that
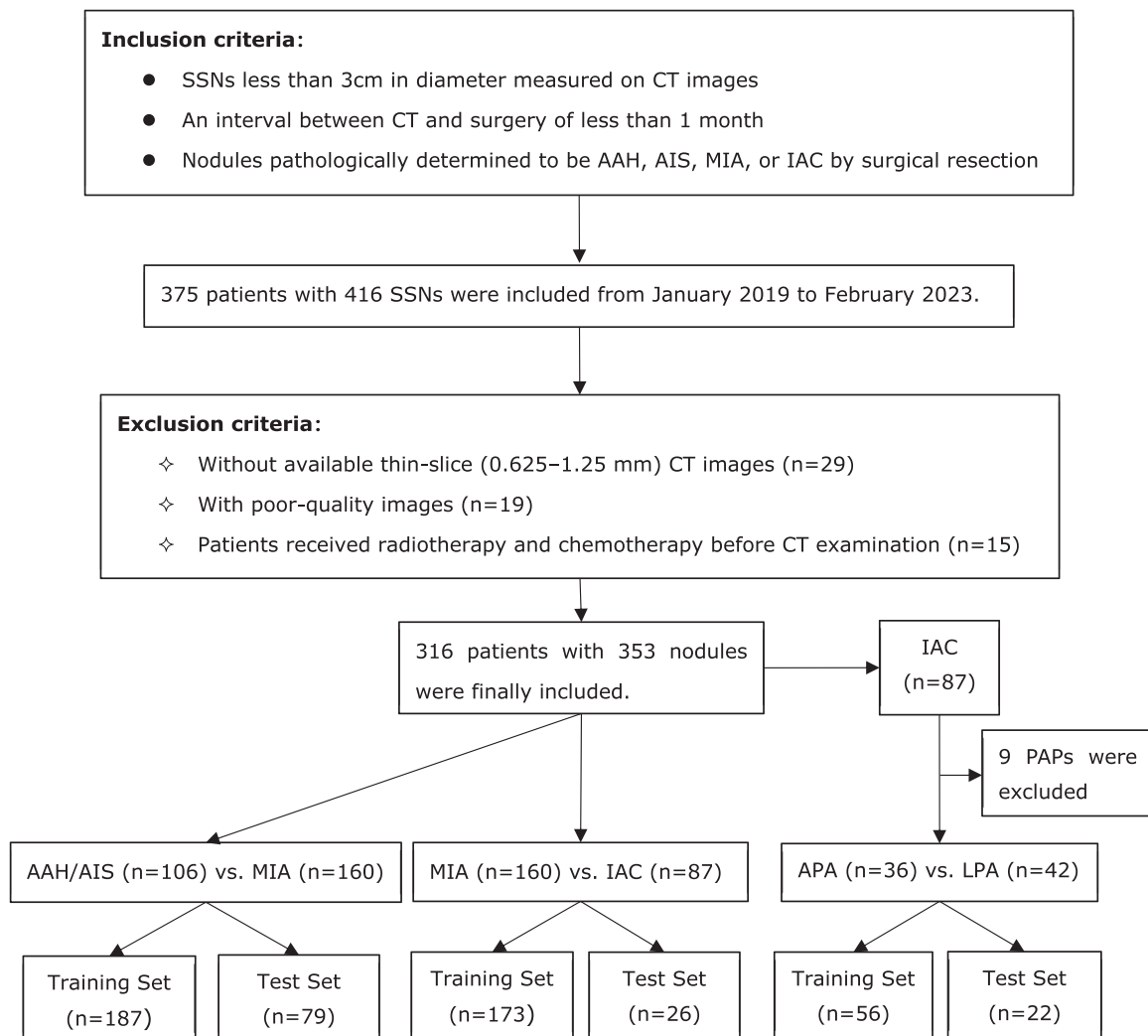

Fig. 1. Flowchart of study population. SSNs, subsolid nodules; AAH, atypical adenomatous hyperplasia; AIS, adenocarcinoma in situ; MIA, microinvasive adenocarcinoma; IAC, invasive adenocarcinoma; LPA, lepidic predominant adenocarcinoma; APA, acinar predominant adenocarcinoma; PAP, papillary predominant adenocarcinoma.

Table 1
Clinical factors and CT imaging features between AAH/AIS and MIA both in the training set and test set.

Characteristics		Training set			Test set		
		AAH/AIS (n=75)	MIA (n=112)	P value	AAH/AIS (n=31)	MIA (n=48)	P value
Gender	Female	57 (76.0 %)	82 (73.2 %)	0.797	19 (61.3 %)	32 (66.7 %)	0.805
	Male	18 (24.0 %)	30 (26.8 %)		12 (38.7 %)	16 (33.3 %)	
Age (y)	Mean ± SD	53±13	52±11	0.388	50±10	51±12	0.722
Smoke	Yes	28 (37.8 %)	51 (45.5 %)	0.299	15 (45.5 %)	25 (52.1 %)	0.748
	No	46 (62.2 %)	61 (54.5 %)		16 (51.6 %)	23 (47.9 %)	
Diameter (mm)	Mean ± SD	8.6±3.0	10.4±3.7	0.000*	8.4±3.3	9.5±3.3	0.143
CT value (HU)	Mean ± SD	-544.1±147.4	-490.4±148.3	0.015*	-575±123.9	-473.6±200.2	0.012*
Lobulation	Absent	40 (53.3 %)	21 (18.8 %)	0.000*	16 (51.6 %)	12 (25.0 %)	0.030*
	Present	35 (46.7 %)	91 (81.2 %)		15 (48.4 %)	36 (75.0 %)	
Spiculation	Absent	68 (90.7 %)	87 (77.7 %)	0.035*	27 (87.1 %)	35 (72.9 %)	0.224
	Present	7 (9.3 %)	25 (22.3 %)		4 (12.9 %)	13 (27.1 %)	
The GGN-vessel relationship	Type I	28 (37.3 %)	10 (8.9 %)	0.000*	14 (45.2 %)	11 (22.9 %)	0.000*
	Type II	36 (48.0 %)	28 (25.0 %)		15 (48.4 %)	11 (22.9 %)	
	Type III	1 (1.3 %)	11 (9.8 %)		0 (0.0 %)	7 (14.6 %)	
	Type IV	10 (13.3 %)	63 (56.2 %)		2 (6.5 %)	19 (39.6 %)	
Pleural indentation	Absent	60 (80.0 %)	76 (67.9 %)	0.097	25 (80.6 %)	31 (64.6 %)	0.200
	Present	15 (20.0 %)	36 (32.1 %)		6 (19.4 %)	17 (35.4 %)	
Crescent sign	Absent	63 (84.0 %)	86 (76.8 %)	0.310	27 (87.1 %)	40 (83.3 %)	0.893
	Present	12 (16.0 %)	26 (23.2 %)		4 (12.9 %)	8 (16.7 %)	
Vacuole sign	Absent	66 (88.0 %)	91 (81.2 %)	0.303	30 (96.8 %)	38 (79.2 %)	0.061
	Present	9 (12.0 %)	21 (18.8 %)		1 (3.2 %)	10 (20.8 %)	
Air bronchogram	Absent	70 (93.3 %)	96 (85.7 %)	0.168	30 (96.8 %)	40 (83.3 %)	0.141
	Present	5 (6.7 %)	16 (14.3 %)		1 (3.2 %)	8 (16.7 %)	
Solid component	Absent	55 (73.3 %)	67 (59.8 %)	0.081	26 (83.9 %)	27 (56.2 %)	0.021*
	Present	20 (26.7 %)	45 (40.2 %)		5 (16.1 %)	21 (43.8 %)	
Solid component size (mm)	Median (25 %,75 %)	0.0 (0.0, 1.0)	0.0 (0.0, 2.8)	0.020*	0.0 (0.0, 0.0)	0.0 (0.0, 3.1)	0.006*
Consolidation tumor ratio (CTR) (%)	Median (25 %,75 %)	0.0 (0.0, 12.0)	0.0 (0.0, 27.3)	0.048*	0.0 (0.0, 0.0)	0.0 (0.0, 31.2)	0.004*

Note: * indicates *P* < 0.05. AAH, atypical adenomatous hyperplasia; AIS, adenocarcinoma in situ; MIA, microinvasive adenocarcinoma.

lobulation, the GGN-vessel relationship, diameter, CT value and CTR were the significant features of the clinical model in distinguishing AAH/AIS from MIA with AUCs of 0.837 (95 % CI, 0.778–0.896) and 0.796 (95 % CI, 0.692–0.879) in the training set and the test set, respectively (Fig. 2). The univariate analysis showed that age, diameter, CT value, spiculation, the GGN-vessel relationship, pleural indentation, solid component, solid component size and CTR were significantly different in the training set between MIA group and IAC group (Table 2). Through multivariate analysis, the clinical model based on age, CT value and CTR were constructed for classification of MIA and IAC with AUCs of 0.764 (95 % CI, 0.692–0.836) and 0.710 (95 % CI, 0.593–0.810) in the training set and the test set, respectively (Fig. 3).

3.3.2. Radiomics feature selection and model construction

For feature selection, 968 features showed good interobserver reproducibility (ICC≥0.80) and were selected for further analysis. The significant radiomics features were retained after the mRMR algorithm

and LASSO analysis (Fig. 4), which were further used to calculate the rad-score. The formulas of the rad-scores was presented in Supplementary Material I. The radiomics model for classification of AAH/AIS and MIA (rad-score1) were constructed with AUCs of 0.772 (95 % CI, 0.705–0.830) and 0.751 (95 % CI, 0.641–0.842) in the training set and the test set, respectively (Fig. 2). The radiomics model for classification of MIA and IAC (rad-score2) showed good performance with AUCs of 0.861 (95 % CI, 0.801–0.909) and 0.857 (95 % CI, 0.757–0.928) in the training set and the test set, respectively (Fig. 3).

3.3.3. Combined model and nomogram

The combined model for classification of AAH/AIS and MIA based on the significant features included rad-score, lobulation, the GGN-vessel relationship, diameter, CT value and CTR showed the best performance with AUCs of 0.841 (95 % CI, 0.783–0.898) and 0.827 (95 % CI, 0.725–0.903) in the training set and the test set, respectively (Fig. 2). The Delong's test showed that in the training set, the AUC of the clinical
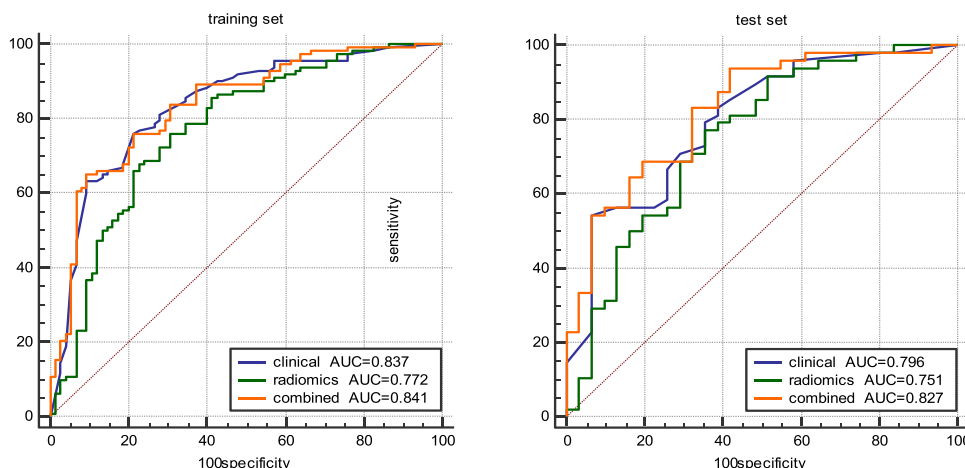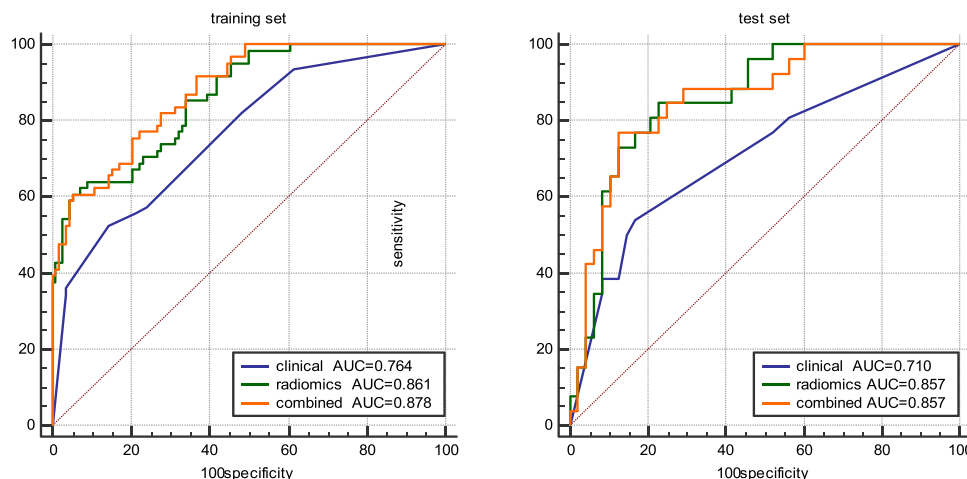

Fig. 2. The ROC curve of clinical model, radiomics model and combined model for AAH/AIS versus MIA in the training set and test set.

Table 2

Clinical factors and CT imaging features between MIA and IAC both in the training set and test set.

Characteristics		Training set			Test set		
		MIA (n=112)	IAC (n=61)	P value	MIA (n=48)	IAC (n=26)	P value
Gender	Female	83 (74.1 %)	39 (63.9 %)	0.220	31 (64.6 %)	18 (69.2 %)	0.884
	Male	29 (25.9 %)	22 (36.1 %)		17 (35.4 %)	8 (30.8 %)	
Age (y)	Mean ± SD	51±11	57±10	0.000b*	53±12	61±8	0.005*
Smoke	Yes	53 (47.3 %)	34 (55.7 %)	0.290	23 (47.9 %)	16 (61.5 %)	0.263
	No	59 (52.7 %)	27 (44.3 %)		25 (52.1 %)	10 (38.5 %)	
Diameter (mm)	Mean ± SD	10.3±3.7	13.7±5.3	0.000*	9.9±3.2	14.0±5.2	0.000*
CT value (HU)	Mean ± SD	-478.5±167.6	-322.9±232.7	0.000b*	-501.4±159.7	-358.4±180.1	0.000*
Lobulation	Absent	22 (19.6 %)	8 (13.1 %)	0.382	11 (22.9 %)	4 (15.4 %)	0.641
	Present	90 (80.4 %)	53 (86.9 %)		37 (77.1 %)	22 (84.6 %)	
Spiculation	Absent	82 (73.2 %)	34 (55.7 %)	0.030*	40 (83.3 %)	11 (42.3 %)	0.001*
	Present	30 (26.8 %)	27 (44.3 %)		8 (16.7 %)	15 (57.7 %)	
The GGN-vessel relationship	Type I	15 (13.4 %)	1 (1.6 %)	0.005*	6 (12.5 %)	0 (0.0 %)	0.004*
	Type II	24 (21.4 %)	6 (9.8 %)		15 (31.2 %)	1 (3.8 %)	
	Type III	14 (12.5 %)	7 (11.5 %)		4 (8.3 %)	2 (7.7 %)	
	Type IV	59 (52.7 %)	47 (77.0 %)		23 (47.9 %)	23 (88.5 %)	
Pleural indentation	Absent	73 (65.2 %)	26 (42.6 %)	0.007*	34 (70.8 %)	16 (61.5 %)	0.579
	Present	39 (34.8 %)	35 (57.4 %)		14 (29.2 %)	10 (38.5 %)	
Crescent sign	Absent	85 (75.9 %)	50 (82.0 %)	0.465	41 (85.4 %)	21 (80.8 %)	0.851
	Present	27 (24.1 %)	11 (18.0 %)		7 (14.6 %)	5 (19.2 %)	
Vacuole sign	Absent	92 (82.1 %)	49 (80.3 %)	0.929	37 (77.1 %)	22 (84.6 %)	0.641
	Present	20 (17.9 %)	12 (19.7 %)		11 (22.9 %)	4 (15.4 %)	
Air bronchogram	Absent	93 (83.0 %)	45 (73.8 %)	0.211	43 (89.6 %)	16 (61.5 %)	0.010*
	Present	19 (17.0 %)	16 (26.2 %)		5 (10.4 %)	10 (38.5 %)	
Solid component	Absent	59 (52.7 %)	16 (26.2 %)	0.001*	35 (72.9 %)	7 (26.9 %)	0.000*
	Present	53 (47.3 %)	45 (73.8 %)		13 (27.1 %)	19 (73.1 %)	
Solid component size (mm)	Median (25 %,75 %)	0.0 (0.0, 3.1)	4.5 (0.0, 7.4)	0.000*	0.0 (0.0, 2.0)	3.8 (0.0, 5.7)	0.000*
Consolidation tumor ratio (CTR) (%)	Median (25 %,75 %)	0.0 (0.0, 30.5)	30.8 (0.0, 57.6)	0.000*	0.0 (0.0, 17.4)	25.6 (0.0, 40.3)	0.000*

Note: * indicates $P < 0.05$. MIA, microinvasive adenocarcinoma; IAC, invasive adenocarcinoma.

Fig. 3. The ROC curve of clinical model, radiomics model and combined model for MIA versus IAC in the training set and test set.

model was greater than that of the radiomics model ($P = 0.05$), and the combined model significantly improved the diagnostic efficiency of the radiomics model ($P = 0.021$). However, there was no significant difference in AUCs between clinical model and combined model ($P = 0.771$). In the test set, the AUCs of the combined model and the radiomics model were close to statistical significance ($P = 0.068$).

For distinguishing MIA from IAC, the combined model based on rad-score, age, CT value and CTR showed the best performance with AUCs of 0.878 (95 % CI, 0.829–0.928) and 0.857 (95 % CI, 0.757–0.928) in the training set and the test set, respectively (Fig. 3). The AUCs of the combined model in the training set and the test set were greater than those of the clinical model ($P = 0.0001$, 0.0015), and the AUCs of the radiomics model in the training set and the test set were also greater than those of the clinical model ($P = 0.0063$, 0.013). However, there was no significant difference in AUC between the combined model and the radiomics model ($P = 0.0965$, 1).

The optimal nomograms of AAH/AIS versus MIA (nomoscore1) and MIA versus IAC (nomoscore2) were constructed respectively based on the combined models (Fig. 5 and Fig. 6), the formulas of which were presented in Supplementary Material II.

3.4. IAC subtype classification model construction

We constructed the IAC subtype classification model separately using the same method described above. There were no significant differences in clinical features between LPA and APA (Table 3), and then ten radiomics features were retained to construct the radiomics model, which showed good performance (The AUCs were 0.926 and 0.792 in training set and the test set respectively) in differentiating LPA from APA (Fig. 7).
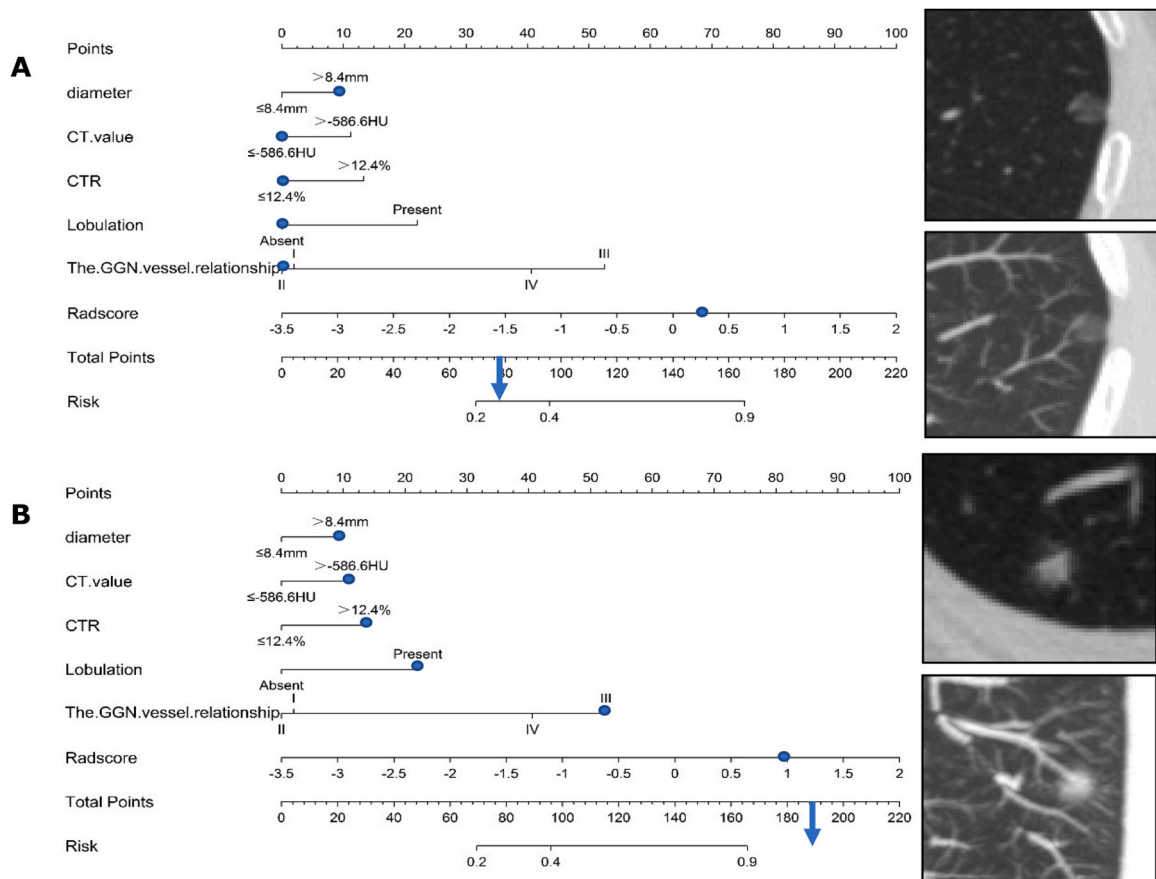
A. AAH/AIS vs. MIA
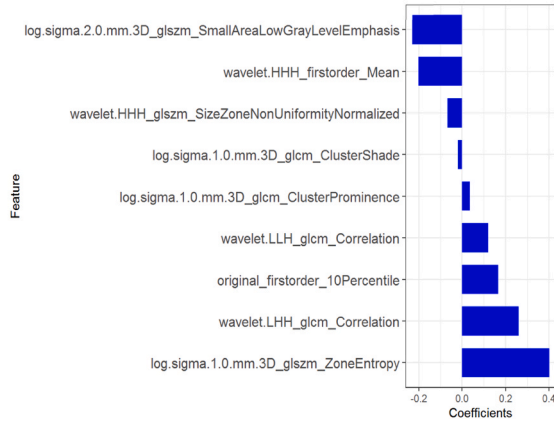
B. MIA vs. IAC
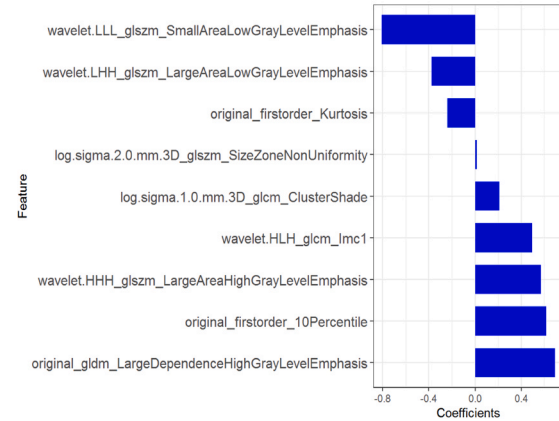
Fig. 4. The significant radiomics features and their coefficients of AAH/AIS versus MIA (A) and MIA versus IAC (B).


Fig. 5. The nomogram of AAH/AIS versus MIA. A. Sample A has a total score of 78, corresponding to a low probability (27 %) of MIA. Sample A is a pure ground glass nodule with type II vessel-GGN relationship on CT images, and finally was pathological confirmed as AAH. B. sample B has a total score of 189, corresponding to a high probability (> 90 %) of MIA. Sample B is a mix ground glass nodule with type III vessel-GGN relationship and lobulation on CT images, and finally was pathological confirmed as MIA.

4. Discussion

The invasiveness and pathological subtypes of SSNs are related to the prognosis, clinical decision and treatment. In this study, we established models based on CT radiomics and clinical features that can accurately differentiate AAH/AIS from MIA and differentiate MIA from IAC, which is helpful to guide the clinical follow-up and treatment of patients with SSNs more reasonably. In addition, we also established the IAC subtypes classification model and found that clinical features had low diagnostic accuracy in distinguishing LPA from APA, while the radiomics model showed good performance in differentiating LPA from APA.

We constructed the combined model of AAH/AIS versus MIA based on five clinical features (the GGN-vessel relationship, lobulation, CT value, CTR and diameter) and rad-score. The clinical model performed better than the radiomics model, but the combined model did not significantly improve the performance for classification of AAH/AIS and MIA compared with the clinical model, indicating that clinical features are very important in distinguishing AAH/AIS from MIA, especially the
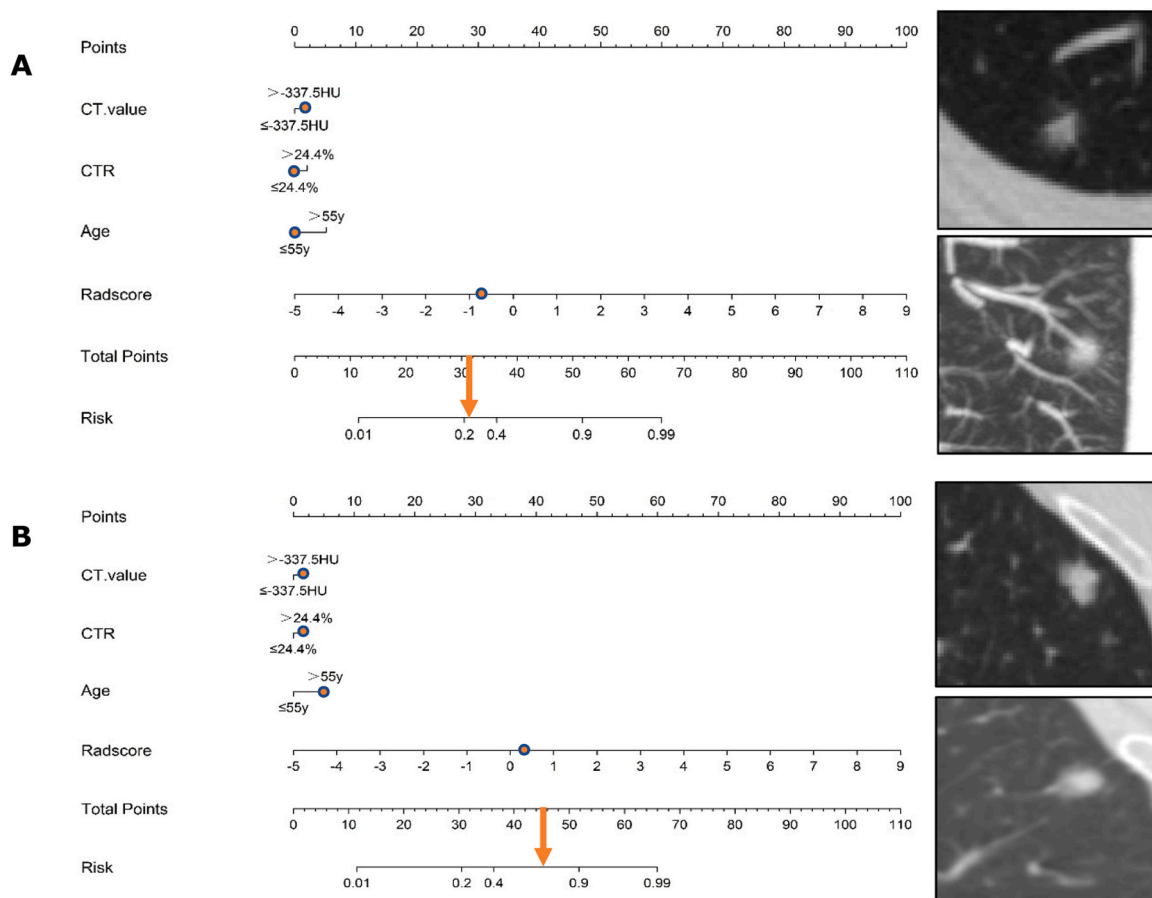
Fig. 6. The nomogram of MIA versus IAC. A. Sample A has a total score of 31.5, corresponding to a low probability (22 %) of IAC. Sample A is a mix ground glass nodule on CT images, and finally was pathological confirmed as MIA. B. sample B has a total score of 45.5, corresponding to a high probability (70 %) of IAC. Sample B is also a mix ground glass nodule shown on CT images, and finally was pathological confirmed as IAC.

Table 3
Clinical factors and CT imaging features between LPA and APA both in training set and test set.

Characteristics		Training set			Test set		
		LPA (n=30)	APA (n=26)	P value	LPA (n=12)	APA (n=10)	P value
Gender	Female	16 (53.3 %)	20 (76.9 %)	0.119	11 (91.7 %)	6 (60.0 %)	0.210
	Male	14 (46.7 %)	6 (23.1 %)		1 (8.3 %)	4 (40.0 %)	
Age (y)	Mean ± SD	60±10	58±10	0.419	56 ±10	53±8	0.402
Smoke	Yes	14 (46.7 %)	15 (57.7 %)	0.410	9 (75.0 %)	7 (70.0 %)	1.000
	No	16 (53.3 %)	11 (42.3 %)		3 (25.0 %)	3 (30.0 %)	
Diameter (mm)	Mean ± SD	16.4±6.8	11.9±3.0	0.002b*	14.1±4.4	12.1±3.1	0.215
CT value (HU)	Mean ± SD	-360±219.7	-311±200.5	0.386b	-412±256.6	-331.5±216.9	0.432
Lobulation	Absent	4 (13.3 %)	4 (15.4 %)	1.000	2 (16.7 %)	2 (20.0 %)	1.000
	Present	26 (86.7 %)	22 (84.6 %)		10 (83.3 %)	8 (80.0 %)	
Spiculation	Absent	15 (50.0 %)	14 (53.8 %)	0.985	6 (50.0 %)	7 (70.0 %)	0.607
	Present	15 (50.0 %)	12 (46.2 %)		6 (50.0 %)	3 (30.0 %)	
The GGN-vessel relationship	Type I	0 (0.0 %)	1 (3.8 %)	0.410	0 (0.0 %)	0 (0.0 %)	0.682
	Type II	2 (6.7 %)	1 (3.8 %)		1 (8.3 %)	2 (20.0 %)	
	Type III	4 (13.3 %)	1 (3.8 %)		3 (25.0 %)	1 (10.0 %)	
	Type IV	24 (80.0 %)	23 (88.5 %)		8 (66.7 %)	7 (70.0 %)	
Pleural indentation	Absent	10 (33.3 %)	14 (53.8 %)	0.202	7 (58.3 %)	6 (60.0 %)	1.000
	Present	20 (66.7 %)	12 (46.2 %)		5 (41.7 %)	4 (40.0 %)	
Crescent sign	Absent	24 (80.0 %)	23 (88.5 %)	0.621	10 (83.3 %)	8 (80.0 %)	1.000
	Present	6 (20.0 %)	3 (11.5 %)		2 (16.7 %)	2 (20.0 %)	
Vacuole sign	Absent	23 (76.7 %)	21 (80.8 %)	0.963	9 (75.0 %)	9 (90.0 %)	0.724
	Present	7 (23.3 %)	5 (19.2 %)		3 (25.0 %)	1 (10.0 %)	
Air bronchogram	Absent	18 (60.0 %)	17 (65.4 %)	0.890	9 (75.0 %)	9 (90.0 %)	0.724
	Present	12 (40.0 %)	9 (34.6 %)		3 (25.0 %)	1 (10.0 %)	
Solid component	Absent	8 (26.7 %)	6 (23.1 %)	1.000	4 (33.3 %)	4 (40.0 %)	1.000
	Present	22 (73.3 %)	20 (76.9 %)		8 (66.7 %)	6 (60.0 %)	
Solid component size (mm)	Median (25 %,75 %)	4.3 (0.0, 8.1)	3.9 (1.4, 6.4)	0.772	2.8 (0.0, 5.4)	4.3 (0.0, 5.5)	0.866
Consolidation tumor ratio (CTR) (%)	Median (25 %,75 %)	25.2 (0.0, 56.6)	31.6 (9.5, 49.3)	0.608	25.7 (0.0, 39.5)	31.4 (0.0, 52.2)	0.787

Note: LPA, Lepidic Predominant Adenocarcinoma; APA, Acinar Predominant Adenocarcinoma; * indicates $P < 0.05$.
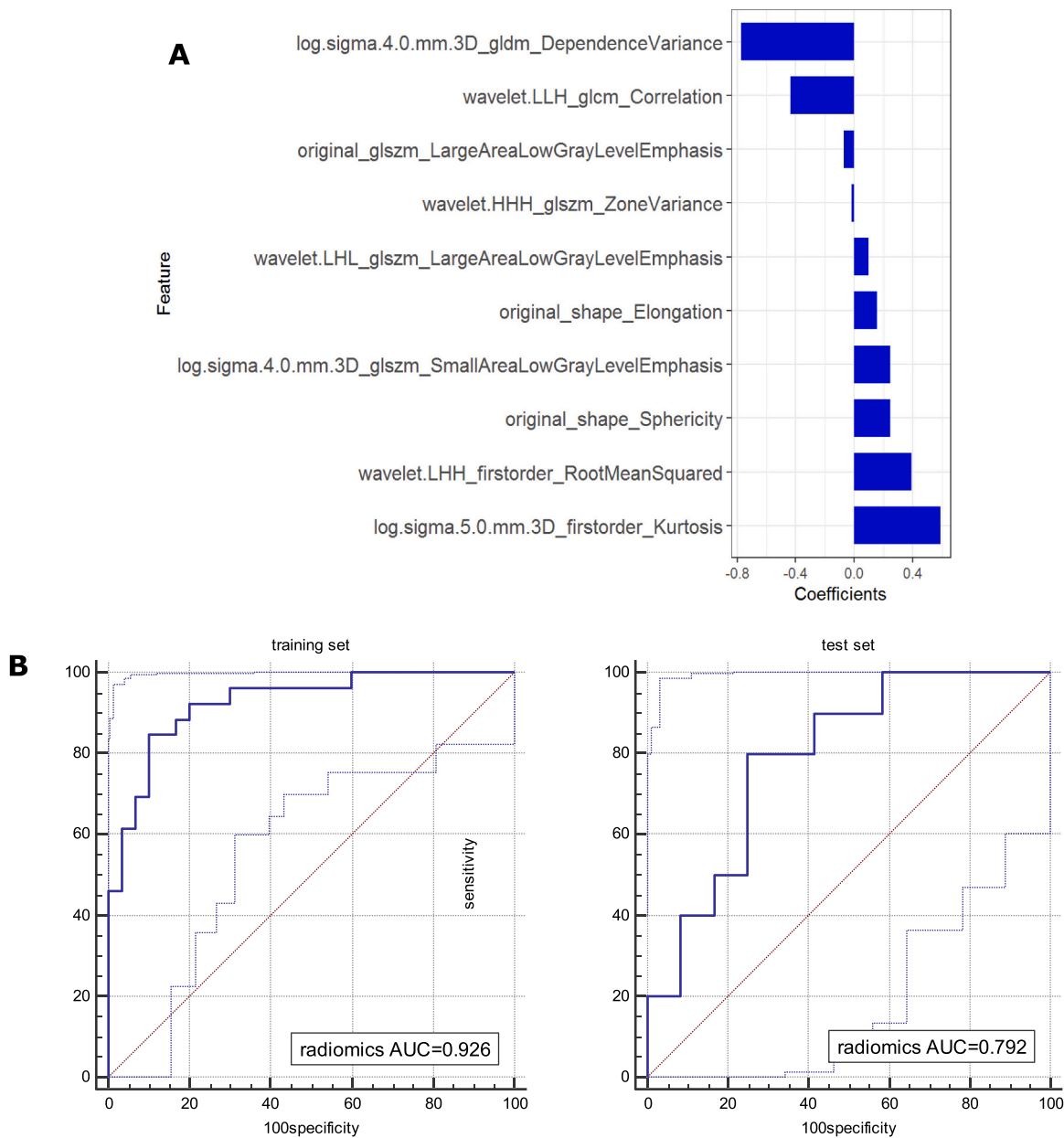
Fig. 7. The radiomics model for classification of LPA and APA. A. the significant radiomics features and their coefficients. B. the ROC curves of the radiomics model in the training set and test set.

GGN-vessel relationship, which contributed the most. Previous studies have found that the GGN-vessel relationship can effectively predict the invasiveness of GGNs. The GGN-vessel relationship reflects the influence of tumor infiltrating components of nodules on peripheral blood vessels and interstitial fiber hyperplasia is the main factor to type III and IV vascular changes [22]. MIA/IAC have pathologically infiltrating components as opposed to AAH/AIS, and thus are prone to present as type III or IV GGN-vessel relationship. Lobulation is caused by the different growth rate in all directions and the contraction of the internal structure of the tumor. Previous studies have also reported that the appearance of lobulation often indicates high risk of aggressive nodules [13,23,24], which is consistent with our initial expectations because of the more aggressive behavior of the latter. Moreover, we found that diameter greater than 8.4 mm indicates possible MIA, which is similar to the findings of Kim et al. [25].

Intriguingly, the radiomics model performed better than the clinical model, and the combined model did not improve the performance for classification of MIA and IAC in the test set compared with the radiomics model, suggesting that radiomics can mine more quantitative data that cannot be identified by naked eye. Small Area Low Gray Level Emphasis (SALGLE) and Large Dependence High Gray Level Emphasis (LDHGLE) contributed most to the rad-score, the differences of which suggested that the image texture of IAC nodules is rougher and the proportion of high gray value distribution is larger. CTR is an important indicator to identify the invasiveness of SSNs. In this study, it was found that the critical value of the CTR for distinguishing MIA from IAC was 24.4 %, which was similar to the findings of Suzuki et al.[21]. Type III and type IV GGN-vessel relationship were more common in MIA and IAC. However, the GGN-vessel relationship was not included in the classification model of MIA versus IAC in this study, indicating that distinguishing type III and type IV is less helpful to predict the invasiveness of nodules.

Previous studies found that CT image features could not effectively identify different pathological subtypes of IAC [26,27], which was consistent with our findings. The radiomics model based on ten features

can effectively distinguish between LPA and APA. Gray Level Dependence Matrix (GLDM), Dependence Variance and First order Kurtosis contributed most significantly to the model, suggesting that there were differences in gray distribution and inhomogeneity of the two subtypes on CT images. Park et al. supposed that a series of radiomics features, including Root Mean Squared (RMS), could distinguish LPA from other pattern-predominant IAC [26], partly consistent with our findings. RMS suggested the effect of volume-confounding. The significant differences in RMS reflected that APA had more heterogeneous and complex voxels, which might correspond to its high-grade pathological growth pattern.

This study has some limitations. First, although we used the data from two centers, the sample of this study was still small and this study was lack of external validation. A larger sample from other centers would be used to further confirm the generalization of the model in the next step. Second, in this study, we used the pathological types of nodules as the classification standard for invasiveness, without predicting the behavioral invasiveness of nodules (growth rate, changes in solid components, etc.). Thus, more samples with follow-up CT data will be collected to further confirm the value of radiomics and clinical features in predicting the invasiveness of SSNs. Finally, it was a retrospective study with selection bias, and a multi-center prospective study would be considered in our future study.

5. Conclusion

The invasiveness-prediction nomograms based on CT radiomics and clinical features could accurately evaluate the invasiveness of SSNs and radiomics is of great value of disguising LPA from APA, which might improve the efficiency of lung cancer screening and providing a theoretical basis for individualized and accurate medical treatment of patients with SSNs.

Funding statement

Ethical statement

We ensure that the work described has been carried out in accordance with The Code of Ethics of the World Medical Association (Declaration of Helsinki) for experiments involving humans. The manuscript is in line with the Recommendations for the Conduct, Reporting, Editing and Publication of Scholarly Work in Medical Journals.

This retrospective study was approved by the Ethics Committees of Second Affiliated Hospital of the Shantou University Medical College and Foshan First People's Hospital, and the requirement for informed consent was waived due to the retrospective nature of the study.

CRediT authorship contribution statement

Zijie Fu: Methodology, Data curation. **Yan Lin:** Writing – review & editing, Validation, Supervision, Resources. **Aizhen Pan:** Writing – review & editing, Resources. **Zhiheng Li:** Writing – review & editing. **Miaozhi Liu:** Writing – original draft, Visualization, Methodology, Investigation, Formal analysis, Data curation, Conceptualization. **Zhifeng Xu:** Resources, Data curation. **Rui Duan:** Resources, Data curation.

Declaration of Competing Interest

The authors declare that they have no known competing financial interests or personal relationships that could have appeared to influence the work reported in this paper.

Acknowledgements

Appendix A. Supporting information

Supplementary data associated with this article can be found in the online version at doi:10.1016/j.ejro.2024.100584.

References

[1] H. Sung, J. Ferlay, R.L. Siegel, et al., Global Cancer Statistics 2020: GLOBOCAN Estimates of Incidence and Mortality Worldwide for 36 Cancers in 185 Countries, CA Cancer J. Clin. 71 (3) (2021) 209–249.

[2] W.D. Travis, E. Brambilla, M. Noguchi, et al., International Association for the Study of Lung Cancer/American Thoracic Society/European Respiratory Society International Multidisciplinary Classification of Lung Adenocarcinoma, J. Thorac. Oncol. 6 (2) (2011) 244–285.

[3] M.S. Tsao, A.G. Nicholson, J.J. Maleszewski, et al., Introduction to 2021 WHO classification of thoracic tumors, J. Thorac. Oncol. 17 (1) (2022) e1–e4.

[4] M. Jia, S. Yu, L. Cao, et al., Clinicopathologic features and genetic alterations in adenocarcinoma In Situ and minimally invasive adenocarcinoma of the lung: long-term follow-up study of 121 asian patients, Ann. Surg. Oncol. 27 (8) (2020) 3052–3063.

[5] H. Soda, Y. Nakamura, K. Nakatomi, et al., Stepwise progression from ground-glass opacity towards invasive adenocarcinoma: long-term follow-up of radiological findings, Lung Cancer 60 (2) (2008) 298–301.

[6] H. Zhang, T. Si, Z. Guo, Clinicopathologic characteristics of pulmonary ground glass opacity located preoperatively using a Hook-wire guidewire, J. Interv. Med. 3 (2) (2020) 89–92.

[7] W.D. Travis, E. Brambilla, A.G. Nicholson, et al., The 2015 World Health Organization Classification oF Lung Tumors: Impact of Genetic, Clinical and Radiologic Advances since the 2004 Classification, J. Thorac. Oncol. 10 (9) (2015) 1243–1260.

[8] N. Yanagawa, S. Shiono, M. Abiko, et al., New IASLC/ATS/ERS classification and invasive tumor size are predictive of disease recurrence in stage I lung adenocarcinoma, J. Thorac. Oncol. 8 (5) (2013) 612–618.

[9] J. Kou, X. Gu, L. Kang, et al., Correlation analysis of computed tomography features and pathological types of multifocal ground-glass nodular lung adenocarcinoma, Comput. Math. Methods Med. 2022 (2022) 1–10.

[10] S. Murakami, H. Ito, N. Tsubokawa, et al., Prognostic value of the new IASLC/ATS/ ERS classification of clinical stage IA lung adenocarcinoma, Lung Cancer 90 (2) (2015) 199–204.

[11] S. Liu, R. Wang, Y. Zhang, et al., Precise diagnosis of intraoperative frozen section is an effective method to guide resection strategy for peripheral small-sized lung adenocarcinoma, J. Clin. Oncol. 34 (4) (2016) 307–313.

[12] Y.C. Yeh, J. Nitadori, K. Kadota, et al., Using frozen section to identify histological patterns in stage I lung adenocarcinoma of ≤ 3 cm: accuracy and interobserver agreement, Histopathology 66 (7) (2015) 922–938.

[13] M. Yanagawa, M. Tsubamoto, Y. Satoh, et al., Lung adenocarcinoma at CT with 0.25-mm section thickness and a 2048 matrix: high-spatial-resolution imaging for predicting invasiveness, Radiology 297 (2) (2020) 462–471.

[14] S.M. Lee, C.M. Park, J.M. Goo, et al., Invasive pulmonary adenocarcinomas versus preinvasive lesions appearing as ground-glass nodules: differentiation by using CT features, Radiology 268 (1) (2013) 265–273.

[15] H. Sakurai, K. Nakagawa, S. Watanabe, et al., Clinicopathologic features of resected subcentimeter lung cancer, Ann. Thorac. Surg. 99 (5) (2015) 1731–1738.

[16] P. Lambin, E. Rios-Velazquez, R. Leijenaar, et al., Radiomics: extracting more information from medical images using advanced feature analysis, Eur. J. Cancer 48 (4) (2012) 441–446.

[17] P. Lambin, R.T.H. Leijenaar, T.M. Deist, et al., Radiomics: the bridge between medical imaging and personalized medicine, Nat. Rev. Clin. Oncol. 14 (12) (2017) 749–762.

[18] X. Wang, Q. Li, J. Cai, et al., Predicting the invasiveness of lung adenocarcinomas appearing as ground-glass nodule on CT scan using multi-task learning and deep radiomics, Transl. Lung Cancer Res 9 (4) (2020) 1397–1406.

[19] Y. She, L. Zhang, H. Zhu, et al., The predictive value of CT-based radiomics in differentiating indolent from invasive lung adenocarcinoma in patients with pulmonary nodules, Eur. Radio. 28 (5) (2018) 5121–5128.

[20] H. Yu, Z. Chen, Q. Li, et al., Crescent sign for predicting the invasiveness of lung adenocarcinoma with pure ground-glass opacity, Chin. J. Radio. 5 (4) (2021) 403–408.

[21] K. Suzuki, T. Koike, T. Asakawa, et al., A prospective radiological study of thin-section computed tomography to predict pathological noninvasiveness in peripheral clinical IA lung cancer (Japan Clinical Oncology Group 0201), J. Thorac. Oncol. 6 (4) (2011) 751–756.

[22] F. Gao, M. Li, X. Ge, et al., Multi-detector spiral CT study of the relationships between pulmonary ground-glass nodules and blood vessels, Eur. Radiol. 23 (12) (2013) 3271–3277.

[23] H.J. Lee, J.M. Goo, C.H. Lee, et al., Predictive CT findings of malignancy in ground-glass nodules on thin-section chest CT: the effects on radiologist performance, Eur. Radio. 19 (3) (2009) 552–560.

[24] W. Fang, G. Zhang, Y. Yu, et al., Identification of pathological subtypes of early lung adenocarcinoma based on artificial intelligence parameters and CT signs, Biosci. Rep. 42 (1) (2022).

[25] H.K. Kim, Y.S. Choi, K. Kim, et al., Management of ground-glass opacity lesions detected in patients with otherwise operable non-small cell lung cancer, J. Thorac. Oncol. 4 (10) (2009) 1242–1246.

[26] S. Park, S.M. Lee, H.N. Noh, et al., Differentiation of predominant subtypes of lung adenocarcinoma using a quantitative radiomics approach on CT, Eur. Radio. 30 (9) (2020) 4883–4892.

[27] H.Y. Lee, S.W. Lee, K.S. Lee, et al., Role of CT and PET imaging in predicting tumor recurrence and survival in patients with lung adenocarcinoma: a comparison with the international association for the study of lung cancer/american thoracic society/european respiratory society classification of lung adenocarcinoma, J. Thorac. Oncol. 10 (12) (2015) 1785–1794.